

Displacement of a three-dimensional immiscible droplet in a duct

By QINJUN KANG¹, DONGXIAO ZHANG²
AND SHIYI CHEN^{3,4}

¹Los Alamos National Laboratory, Los Alamos, NM 87545, USA

²University of Oklahoma, Norman, OK 73019, USA

³The Johns Hopkins University, Baltimore, MD 21218, USA

⁴Peking University, Beijing, China

(Received 2 October 2003 and in revised form 10 June 2005)

The displacement of a three-dimensional immiscible droplet subject to gravitational forces in a duct is studied with the lattice Boltzmann method. The effects of the contact angle and capillary number (the ratio of viscous to surface forces) on droplet dynamics are investigated. It is found that there exists a critical capillary number for a droplet with a given contact angle. When the actual capillary number is smaller than the critical value, the droplet moves along the wall and reaches a steady state. When the capillary number is greater than the critical value, one or more small droplets pinch off from the wall or from the rest of the droplet, depending on the contact angle and the specific value of the capillary number. As the downstream part of the droplet is pinching off, a bottleneck forms and its area continues decreasing until reaching zero. The general trend found in a previous two-dimensional study that the critical capillary number decreases as the contact angle increases is confirmed. It is shown that at a fixed capillary number above the critical value, increasing the contact angle results in a larger first-detached portion. At a fixed contact angle, increasing the capillary number results in an increase of the size of the first detached droplet for $\theta = 78^\circ$ and $\theta = 90^\circ$, but a decrease for $\theta = 118^\circ$. It is also found that the droplet is stretched longer as the capillary number becomes larger. For a detaching droplet, the maximal velocity value occurs near the bottleneck between the up- and downstream parts of the droplet and the shear stress there reaches a local maximum. The three-dimensional effects are most clearly seen for $\theta = 90^\circ$, where the wetted length and wetted area vary in the opposite direction and the shape of the interface between the wall and the droplet is distorted severely from the original round shape.

1. Introduction

The displacement of immiscible fluids is an important phenomenon for a wide range of engineering applications, including oil recovery, transport of non-aqueous-phase liquid contamination in the soil, and geologic sequestration of carbon dioxide. Immiscible displacement in capillary tubes is a moving contact-line problem, which challenges the classical hydrodynamic methods and has attracted the attention of many investigators (e.g. Dussan V. & Davis 1974; Dussan V. 1976, 1979; Hocking 1976, 1977; de Gennes 1985; Jansons 1985; Cox 1986; Koplik, Banavar & Willemsen 1988; Zhou & Sheng 1990; Shikhmurzaev 1997; Chen, Jasnow & Vinals 2000; Jacqmin 2000; Freund 2003; Briant, Wagner & Yeomans 2004; Briant & Yeomans 2004). Even

though it has been shown that the no-slip boundary condition and the moving contact line are kinematically compatible (Dussan V. & Davis 1974), the theoretical analyses of such a liquid/liquid/solid system on the basis of the classical approach, with a sharp interface and a no-slip boundary condition, lead to a non-integrable stress singularity at the contact line.

To remove the singularity, the model of the fluids must be altered. One obvious way is to relieve the no-slip boundary condition (Dussan V. 1979). It has been pointed out that the selection of slip boundary conditions is endless. Although the flow field very close to the contact line was different for different models, they were identical when examined on a length scale that characterized the overall geometry of the fluids (Dussan V. 1979), meaning that no macroscopic measurement can be used to infer microscopic properties. More recent studies (Chen *et al.* 2000; Jacqmin 2000; Briant *et al.* 2004; Briant & Yeomans 2004) have provided alternative explanations of contact line motion which do not rely on the breakdown of the no-slip condition and have shown that effective slip of the interface relative to the wall may be generated by mechanisms missing from sharp interface treatments. In these studies, the fluid–fluid interface is not a material line and can be moved diffusively as well as by advection. As a result, the moving contact line can exist, at least mathematically, even with strict no-slip conditions for the velocity. The velocity fields obtained from these studies have the same outer behaviour, but different inner behaviours and physics as those of the classical studies.

The method Briant *et al.* (2004) and Briant & Yeomans (2004) used is a lattice Boltzmann (LB) multiphase multicomponent model. The LB method is a relatively new numerical method in computational fluid dynamics. Because it is based on microscopic models and mesoscopic kinetic equations, it has the advantage in the study of fluid–flow applications involving interfacial dynamics and complex boundaries (Chen & Doolen 1998). There are rigorous mathematical derivations of the Navier–Stokes equations from LB equations in the nearly incompressible limit (Chen, Chen & Matthaeus 1992). Also available in the literature are grid convergence tests (He *et al.* 1999*b*) and successful applications to flow in porous media, turbulence, multiphase and multicomponent flows, particle suspensions in fluids, heat transfer and chemical reaction (see Chen & Doolen 1998 for a review).

The bounce-back condition at the solid boundary in the LB method has been shown to recover the no-slip velocity condition in the limit of small Knudsen number (Wolfram 1986; Nie, Doolen & Chen 2002). Because of the kinetic nature of the LB equations and bounce-back condition, there is no such singularity in the LB simulation of moving contact-line problems while the no-slip condition is satisfied. Moreover, since this method does not follow each particle as molecular dynamics simulations, it requires significantly less computer time. Grubert & Yeomans (1999) have used a binary LB approach to measure contact angles of small droplets. Briant and colleagues have used an LB model to simulate contact line motion in both liquid–gas systems (Briant *et al.* 2004) and binary fluids (Briant & Yeomans 2004). They find, in agreement with Jacqmin (2000) and Chen *et al.* (2000), a slip mechanism: the relative diffusion of the two fluid components in the vicinity of the contact line. This diffusive transport of fluid can lead to effective slip of the interface of finite width at the contact line.

The objective of this study is to apply another LB multiphase multicomponent model to the problem of the moving contact line, to gain new perspectives on solutions offered in the literature. Among other problems, the displacement of an immiscible droplet adhering to a wall in a channel under external forces is particularly interesting

and challenging because there is a coalescence of contact lines when the droplet detaches from the wall (Schleizer & Bonnecaze 1998; Kang, Zhang & Chen 2002).

Using a boundary-integral method, Schleizer & Bonnecaze (1998) studied the dynamic behaviour and stability of a two-dimensional immiscible droplet subject to shear or pressure-driven flow under conditions where inertial and gravitational forces can be neglected. The droplet is attached to the solid surface, and the two contact lines are either fixed or mobile. To allow the droplet to slip along the wall, they applied an integral form of the Navier-slip model. To avoid introducing an additional phenomenological relationship between the contact angle and the velocity of the contact line, they assumed that the contact angle is independent of the speed of the contact line and is therefore equal to its static value. Hence, in their study, only the limit where there is no contact angle hysteresis is examined. They investigated the effects of contact angle, capillary number (the ratio of viscous to surface forces), droplet size and viscosity ratio on the droplet behaviour. Their simulation results showed that for contact angles less than or equal to 90° , a stable droplet spreads along the wall until a steady shape is reached; the droplet then moves along the wall at a constant velocity. Above a critical capillary number, part of the droplet pinches off leaving behind a smaller attached droplet.

For contact angles greater than 90° , the wetted length between a stable droplet and the wall decreases until a steady shape is reached. They also claimed that above a critical capillary number, the droplet completely detaches for a contact angle of 120° . However, they indicated that it was too difficult to include the coalescence of the contact lines in their numerical method.

In a previous study by Kang *et al.* (2002), we used an LB multiphase model to study the displacement of a two-dimensional immiscible droplet subject to gravitational forces in a channel. We assessed the effects of the contact angle, Bond number (the ratio of gravitational to surface forces), droplet size and the density and viscosity ratios of the droplet to the displacing fluid. Our simulation results indicated that there exists a critical Bond number for a given static contact angle, above which no steadily sliding droplet is observed. The value of the critical Bond number decreases as the contact angle increases. At a Bond number above the critical value, increasing the contact angle results in a larger fraction of the droplet being entrained in the bulk. Most of our results are in line with the simulation results and the assertion by Schleizer & Bonnecaze (1998).

Although the diffusive interface of finite width can overcome the contact-line singularity and gives the same macroscopic droplet behaviour as a slip boundary condition, it cannot pinpoint the physically relevant mechanism in the vicinity of the contact line, which may well be system dependent. For that purpose, nanoscale experiments or extremely large molecular dynamics simulations will be required. In addition, the finite interface width makes it difficult to pinpoint the accurate position of the interface. In the previous study, we set the interface at the place where the two fluids have equal number density.

In this study, we use the same method to investigate the dynamic behaviour of a three-dimensional immiscible droplet in a duct. It is the first study on this subject to our best knowledge. In §2, the multiphase or multicomponent LB model is reviewed. In §3, the details of the simulation set-up and the boundary and initial conditions are presented. In §§4 and 5, the effects of contact angle and capillary number are discussed, respectively. The results are summarized in §6. All figures except figure 1 are plotted using Tecplot. By using bilinear interpolation, it gives smooth contour lines and surfaces for two- and three-dimensional spaces, respectively.

2. Model and theory

There are several LB models used for the study of multiphase and/or multi-component flow. Gunstensen *et al.* (1991) developed a multicomponent LB model based on a two-component lattice gas model. Shan & Chen (1993) proposed an LB model with interparticle potential for multiphase and multicomponent fluid flows. Swift, Osborn & Yeomans (1995) developed an LB multiphase and multicomponent model by using the free-energy approach. He, Chen & Zhang (1999a) proposed an LB multiphase model using the kinetic equation for multiphase flow. As in the previous two-dimensional study, we use the model with interparticle potential because of its convenience in handling fluid/solid interaction.

For completeness, we first review the multiphase or multicomponent LB model proposed by Shan & Chen (1993). In their model, k distribution functions are introduced for a fluid mixture of k fluid components. Each distribution function represents a fluid component and satisfies the evolution equation. The interaction between the particles is included in the kinetics through a set of potentials. The LB equations for the k th component can be written in the following form:

$$f_i^k(\mathbf{x} + \mathbf{e}_i \delta_t, t + \delta_t) - f_i^k(\mathbf{x}, t) = -\frac{f_i^k(\mathbf{x}, t) - f_i^{k(eq)}(\mathbf{x}, t)}{\tau_k}, \quad (2.1)$$

where $f_i^k(\mathbf{x}, t)$ is the number density distribution function in the i th velocity direction for the k th fluid at position \mathbf{x} and time t , and δ_t is the time increment. On the right-hand side, τ_k is the relaxation time of the k th component and is in the lattice unit, and $f_i^{k(eq)}(\mathbf{x}, t)$ is the corresponding equilibrium distribution function. For a three-dimensional 19-speed LB model (D3Q19, where D is the dimension and Q is the number of velocity directions), $f_i^{k(eq)}(\mathbf{x}, t)$ has the following form (Chen *et al.* 1992; Martys & Chen 1996):

$$\left. \begin{aligned} f_0^{k(eq)} &= d_k n_k - \frac{1}{2} n_k \mathbf{u}_k^{eq} \cdot \mathbf{u}_k^{eq}, \\ f_i^{k(eq)} &= \frac{1-d_k}{12} n_k + \frac{1}{6} n_k (\mathbf{e}_i \cdot \mathbf{u}_k^{eq}) + \frac{1}{4} n_k (\mathbf{e}_i \cdot \mathbf{u}_k^{eq})^2 - \frac{1}{12} n_k \mathbf{u}_k^{eq} \cdot \mathbf{u}_k^{eq} \\ &\quad \text{for } i = 1, \dots, 6, \\ f_i^{k(eq)} &= \frac{1-d_k}{24} n_k + \frac{1}{12} n_k (\mathbf{e}_i \cdot \mathbf{u}_k^{eq}) + \frac{1}{8} n_k (\mathbf{e}_i \cdot \mathbf{u}_k^{eq})^2 - \frac{1}{24} n_k \mathbf{u}_k^{eq} \cdot \mathbf{u}_k^{eq} \\ &\quad \text{for } i = 7, \dots, 18. \end{aligned} \right\} \quad (2.2)$$

In the above equations, \mathbf{e}_i are the discrete velocities, which are chosen to be

$$\mathbf{e}_i = \begin{cases} (0, 0, 0), & i = 0, \\ (\pm 1, 0, 0), (0, \pm 1, 0), (0, 0, \pm 1), & i = 1 - 6, \\ (\pm 1, \pm 1, 0), (\pm 1, 0, \pm 1), (0, \pm 1, \pm 1), & i = 7 - 18, \end{cases} \quad (2.3)$$

and d_k is a free parameter, which relates to the sound speed of a region of pure k th component as $(c_s^k)^2 = (1 - d_k)/2$; $n_k = \sum_i f_i^k$ is the number density of the k th component. The mass density of the k th component ρ_k is defined as $\rho_k = m_k n_k = m_k \sum_i f_i^k$, and the fluid velocity of the k th fluid \mathbf{u}_k is defined through $\rho_k \mathbf{u}_k = m_k \sum_i \mathbf{e}_i f_i^k$, where m_k is the molecular mass of the k th component. The parameter \mathbf{u}_k^{eq} is determined by the relation,

$$\rho_k \mathbf{u}_k^{eq} = \rho_k \mathbf{u}' + \tau_k \mathbf{F}_k, \quad (2.4)$$

where \mathbf{u}' is a common velocity on top of which an extra component-specific velocity due to interparticle interaction is added for each component, and $\mathbf{F}_k = \mathbf{F}_{1k} + \mathbf{F}_{2k} + \mathbf{F}_{3k}$

is the total force acting on the k th component, including fluid/fluid interaction \mathbf{F}_{1k} , fluid/solid interaction \mathbf{F}_{2k} , and external force \mathbf{F}_{3k} (Martys & Chen 1996). To conserve momentum at each collision in the absence of interaction (i.e. in the case of $\mathbf{F}_k = 0$), \mathbf{u}' has to satisfy the relation,

$$\mathbf{u}' = \left(\sum_{k=1}^s \frac{\rho_k \mathbf{u}_k}{\tau_k} \right) / \left(\sum_{k=1}^s \frac{\rho_k}{\tau_k} \right). \quad (2.5)$$

The interactive force between particles of the k th component at site \mathbf{x} and the \bar{k} th component at site \mathbf{x}' is assumed to be proportional to the product of their 'effective number density' $\psi_k(n_k)$, defined as a function of local number density. The total fluid/fluid interactive force on the k th component at site \mathbf{x} is

$$\mathbf{F}_{1k}(\mathbf{x}) = -\psi_k(\mathbf{x}) \sum_{\mathbf{x}'} \sum_{\bar{k}=1}^s G_{k\bar{k}}(\mathbf{x}, \mathbf{x}') \psi_{\bar{k}}(\mathbf{x}') (\mathbf{x}' - \mathbf{x}), \quad (2.6)$$

where $G_{k\bar{k}}(\mathbf{x}, \mathbf{x}')$ satisfies $G_{k\bar{k}}(\mathbf{x}, \mathbf{x}') = G_{\bar{k}k}(\mathbf{x}', \mathbf{x})$, and $\psi_k(\mathbf{x})$ is a function of \mathbf{x} through its dependency on n_k . The above form of interaction potential was originally used for single-speed lattices such as the two-dimensional hexagonal and the four-dimensional face-centred hypercubic lattice (FCHC) (Shan & Chen 1993), and only homogeneous isotropic interactions between the nearest neighbours were considered. The interaction potential of the D3Q19 lattice can be obtained with a method adopted by Martys & Chen (1996) to project the interaction potential from the four-dimensional FCHC lattice to the D3Q19 model. The nearest-neighbour interaction in four dimensions corresponds to a potential that couples nearest and next-nearest neighbours in the D3Q19 lattice model. In this case,

$$G_{k\bar{k}}(\mathbf{x}, \mathbf{x}') = \begin{cases} g_{k\bar{k}}, & |\mathbf{x} - \mathbf{x}'| = 1, \\ g_{k\bar{k}}/2, & |\mathbf{x} - \mathbf{x}'| = \sqrt{2}, \\ 0, & \text{otherwise.} \end{cases} \quad (2.7)$$

Here, $g_{k\bar{k}}$ is the strength of the interparticle potential between component k and \bar{k} . The effective number density $\psi_k(n_k)$ is taken as n_k in this study. Other choices will give a different equation of state.

At the fluid/solid interface, the wall is regarded as a phase with a constant number density. The interactive force between the fluid and wall is described as

$$\mathbf{F}_{2k}(\mathbf{x}) = -n_k(\mathbf{x}) \sum_{\mathbf{x}'} g_{kw} n_w(\mathbf{x}') (\mathbf{x}' - \mathbf{x}), \quad (2.8)$$

where n_w is the number density of the wall, which is a constant at the wall and zero elsewhere, and g_{kw} is the interactive strength between component k and the wall. The interactive strength g_{kw} is positive for a non-wetting fluid and negative for a wetting fluid. By adjusting it, we can obtain different wettabilities. Note that \mathbf{F}_{2k} is perpendicular to the wall and will not affect the no-slip boundary condition.

The action of a constant-body force can be simply introduced as

$$\mathbf{F}_{3k} = \rho_k \mathbf{g} = m_k n_k \mathbf{g}, \quad (2.9)$$

where \mathbf{g} is the body force per unit mass.

The Chapman–Enskog expansion procedure can be carried out to obtain the following continuity and momentum equations for the fluid mixture as a single fluid

in the nearly incompressible limit (Shan & Doolen 1996):

$$\frac{\partial \rho}{\partial t} + \nabla \cdot (\rho \mathbf{u}) = 0, \quad (2.10)$$

$$\rho \left[\frac{\partial \mathbf{u}}{\partial t} + (\mathbf{u} \cdot \nabla) \mathbf{u} \right] = -\nabla p + \nabla \cdot [\rho \nu (\nabla \mathbf{u} + (\nabla \mathbf{u})^\top)] + \rho \mathbf{g}, \quad (2.11)$$

where $\rho = \sum_k \rho_k$ is the total density of the fluid mixture, and the whole fluid velocity \mathbf{u} is defined by $\rho \mathbf{u} = \sum_k \rho_k \mathbf{u}_k + \sum_k \mathbf{F}_k/2$ (Shan & Doolen 1995). The pressure is given by $p = \sum_k (1 - d_k) m_k n_k/2 + 3 \sum_{k,\bar{k}} g_{k\bar{k}} \psi_k \psi_{\bar{k}}$, which is generally a non-ideal gas equation of state (Shan & Doolen 1996).

To simulate a multiple component fluid with different component densities, it is appropriate to let $(1 - d_k) m_k$ be a constant. In this study, the different components have the same density. We let $m_k = 1$ and $d_k = 1/3$, which is commonly used in the literature. Then the equation of state can be written as $p = \sum_k n_k/3 + 3 \sum_{k,\bar{k}} g_{k\bar{k}} \psi_k \psi_{\bar{k}}$. The viscosity is given by $\nu = (\sum_k \beta_k \tau_k - 1/2)/3$, where β_k is the mass density concentration of the k th component and is defined as $\rho_k / \sum_k \rho_k$ (Hou *et al.* 1997). Notice that the introduction of fluid/solid interaction has no effect on the macroscopic equations since \mathbf{F}_{2k} exists only at the fluid/solid interface.

This model has been shown to satisfy Galilean invariance (Shan & Doolen 1995). In addition to its convenience in handling fluid/solid interaction, it is also convenient for handling fluids with different densities and viscosities. Although this model does not conserve the net momentum at each site, which is physically plausible because the distant pairwise interactions between phases change the point-wise local momenta at the positions involved in the interactions (Chen & Doolen 1998), the total momentum of the system obtained by summing over the net momenta at every site is still exactly conserved (Shan & Chen 1993). This feature is different from a previous LB multiphase model (Gunstensen *et al.* 1991) where the total local momentum is conserved. It is arguable that this unnecessary conservation might be one reason why that model exhibits unphysical features near interfaces (Chen & Doolen 1998). Furthermore, in the model with interparticle potential, the separation of a two-phase fluid into its components is automatic (Chen & Doolen 1998). Hence, in simulating the displacement of the immiscible droplet with this model, there is no need to track the interface, nor need we make any assumption about the relationship between the contact angle and velocity of the contact line. Also, the coalescence of the contact lines can be demonstrated more easily.

One disadvantage of this LB multiphase/multicomponent model is that although expressions for the surface tension of a single component liquid/gas fluid exist, the surface tension of a multicomponent fluid must be found through simulation. This creates difficulties in applications in which an adjustable surface tension is required (He & Doolen 2002). The difficulties can be relieved by the finding that the dependence of the surface tension on $g_{k\bar{k}}$ is nearly linear (Yang *et al.* 2000).

3. Simulation set-up

The three-dimensional geometry used in our simulations is shown in figure 1, where an immiscible droplet (fluid 2) with volume V is placed into a three-dimensional duct filled with fluid 1. The length of the duct is l , its width is w in the x -direction and h in the y -direction. A_0 is the wetted area between the droplet and the wall; b_0 is the wetted length in the z -direction; a_0 is the droplet height; and θ_1 and θ_2 are the contact angles of fluids 1 and 2, respectively. The contact angle is defined as the

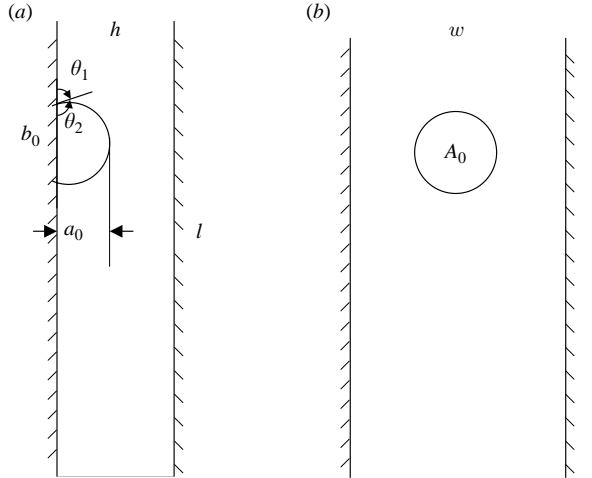


FIGURE 1. Schematic of simulation geometry: (a) (y, z) -plane view, (b) (x, z) -plane view.

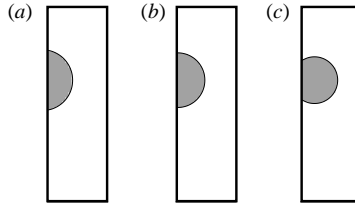


FIGURE 2. Three static contact angles obtained by adjusting g_{2w} : (a) $g_{2w} = -0.02$, $\theta = 78^\circ$, (b) $g_{2w} = 0$, $\theta = 90^\circ$, (c) $g_{2w} = 0.05$, $\theta = 118^\circ$.

angle between a two-fluid interface and a solid surface. As shown in figure 1, each fluid has its own contact angle and the sum of the two must equal 180° . The wetting fluid (the fluid that tends to wet the surface) has a contact angle of less than 90° , and the non-wetting fluid (the fluid that has less affinity for the solid surface) has a contact angle of greater than 90° . In all simulations below, $l = 300$, $h = 40$ and $w = 80$, all in lattice unit spacings, $V/h^3 = 0.2$, $\rho_2/\rho_1 = 1$, $\tau_1 = \tau_2 = 1$, $g_{1w} = -g_{2w}$, $g_{11} = g_{22} = 0$ and $g_{12} = g_{21} = 0.1$. In this study, we consider only the two-fluid system with equal density and viscosity, though this method is equally applicable to systems with different densities and viscosities (Kang *et al.* 2002). Bounce-back boundary conditions are imposed at walls and periodic boundary conditions are applied at $z = 0$ and $z = l$. The flow is induced by a constant body force along the $-z$ -direction.

The static contact angle can be reasonably well predicted by equation (2.8) (Martys & Chen 1996; Kang *et al.* 2002). In the simulation of the static contact angle, no body force is applied. Initially, $b_0 = 2a_0 = 2R$. When a static droplet is obtained, the values of a_0 and b_0 are measured, and R and θ are calculated. The values of g_{1w} and g_{2w} are varied to obtain static droplets with different contact angles. As shown in figure 2, contact angles $\theta_2 = 78^\circ$, 90° and 118° are obtained by letting g_{2w} equal -0.02 , 0 and 0.05 , respectively. For simplicity, hereinafter we refer to θ_2 when we say contact angle or θ .

After a static droplet is achieved at time zero, a constant body force (gravitational force) is applied to both the displacing fluid and the droplet along the $-z$ -direction. In order to compare with the two-dimensional simulations, we define $U = \rho_1 g h^2 / \mu_1$

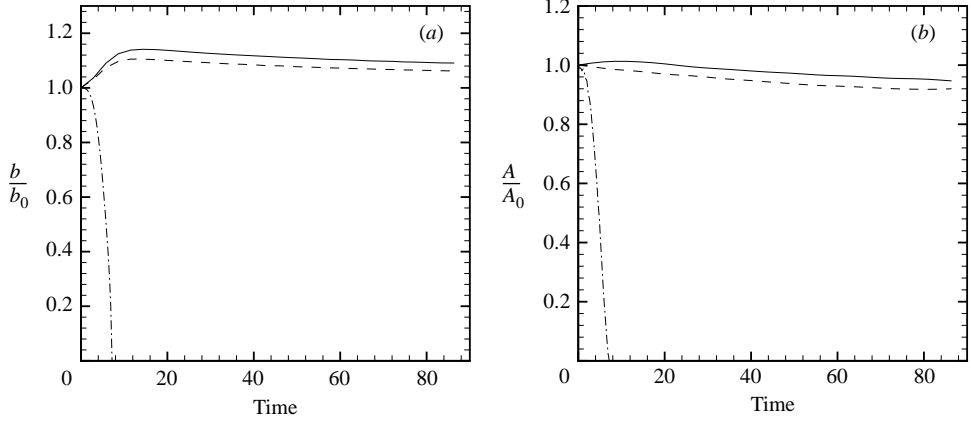


FIGURE 3. Evolution of the dimensionless wetted length b/b_0 and wetted area A/A_0 between the wall and the sliding droplet at three contact angles (—, $\theta = 78^\circ$; ---, 90° ; - · - ·, 118°) and at $Ca = 0.35$, where b_0 and A_0 are the wetted length and wetted area at time 0, respectively. Time is made dimensionless by characteristic time l/U : (a) evolution of b/b_0 , (b) evolution of A/A_0 .

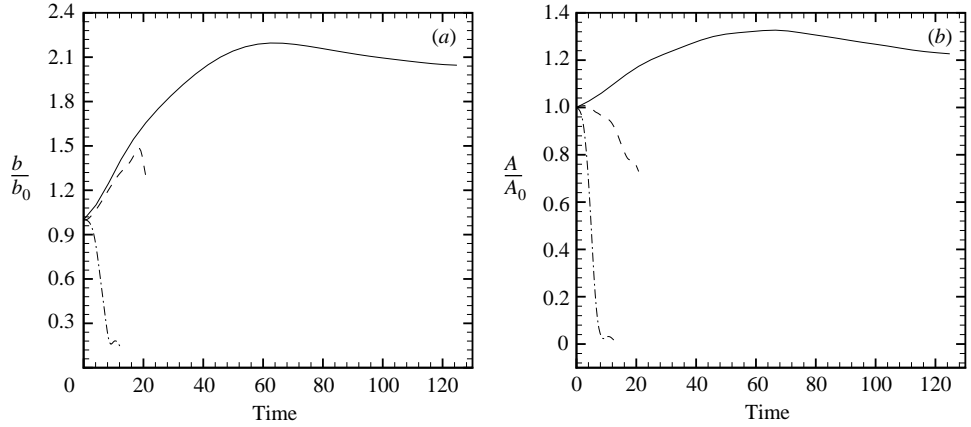
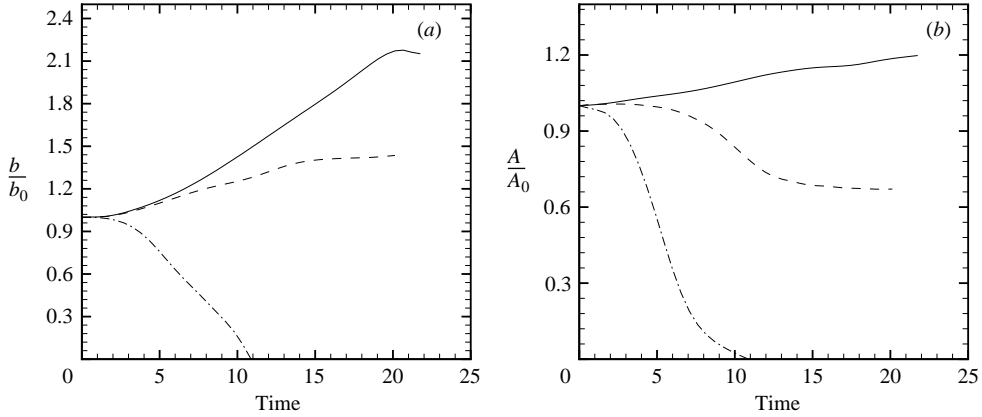
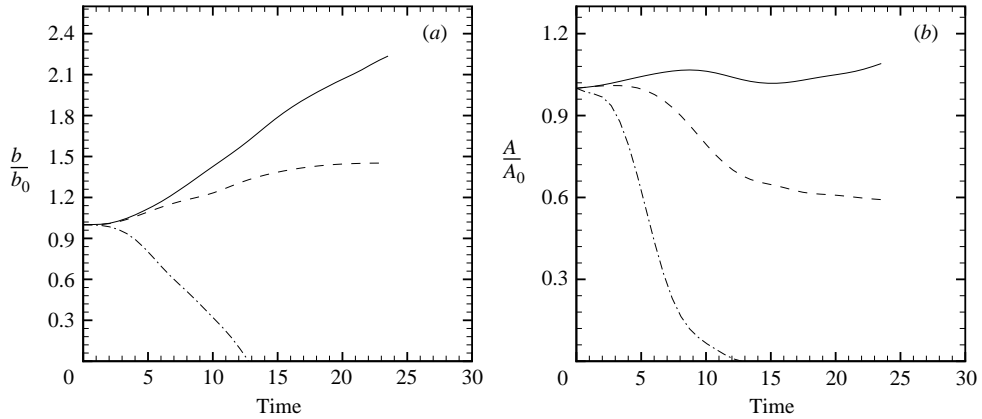


FIGURE 4. As figure 3, but for $Ca = 0.50$.

as the characteristic velocity, and l/U as the characteristic time, where ρ_1 and μ_1 are the density and viscosity of fluid 1, respectively. The capillary number is defined as $Ca = (\mu_1 U / \sigma)(V/h^3) = \rho_1 g V / \sigma h$, where g is the gravitational factor and σ is the surface tension, which is calculated using Laplace's law in bubble tests (see Kang *et al.* 2002 for details). The capillary number is a dimensionless parameter that indicates the ratio of viscous force to interfacial force.

4. Effect of contact angle

Figures 3–6 show the time evolution of the dimensionless wetted length b/b_0 and wetted area A/A_0 between the wall and the sliding droplet at three contact angles ($\theta = 78^\circ$, 90° and 118°) and at four capillary numbers (0.35, 0.50, 0.66 and 0.81). Different capillary numbers are obtained by changing g , the gravitational factor. For

FIGURE 5. As figure 3, but for $Ca = 0.66$.FIGURE 6. As figure 3, but for $Ca = 0.81$.

a given g , we calculate the capillary number by $Ca = \rho_1 g V / \sigma h$ and keep two decimal digits. The capillary number can also be changed by changing the droplet size or the surface tension, but changing the gravitational factor is the most convenient way. Figures 7–10 are the three-dimensional views of dynamical behaviour of the droplet at these three contact angles and different capillary numbers.

At the capillary number of 0.35 (figure 3), for $\theta = 78^\circ$ (wetting case), both wetted length (b/b_0) and wetted area (A/A_0) increase with time at first, then decrease slowly and reach a steady-state value. For $\theta = 90^\circ$, b/b_0 increases with time at first, then decreases, while A/A_0 decreases with time monotonically before it reaches a steady-state value. Here, the steady state is claimed to be reached when the wetted length between the droplet and wall varies less than 0.2% in 1000 successive time steps. Reducing the criteria to 0.1% does not produce a significant change in the steady shape of the droplet. For the case of $\theta = 118^\circ$ (non-wetting case), both b/b_0 and A/A_0 dramatically decrease with time and reaches 0 at time 7.8, when the droplet totally detaches from the wall, as shown in figure 7. In this non-wetting case, the capillary number already exceeds a critical value called the critical capillary number

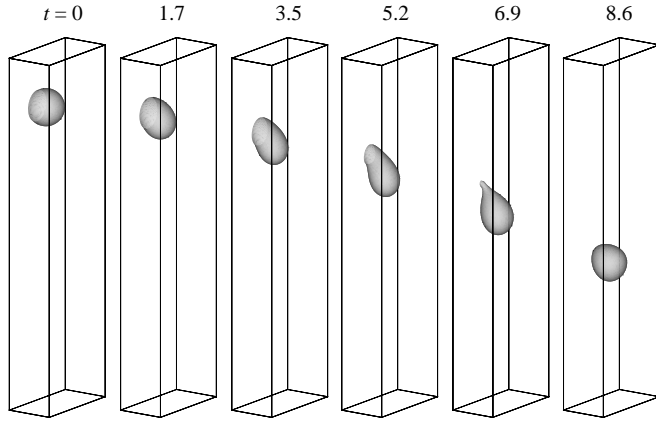


FIGURE 7. Dynamic behaviour of the non-wetting droplet ($\theta = 118^\circ$) at $Ca = 0.35$ (three-dimensional view), the entire droplet detaches from the wall.

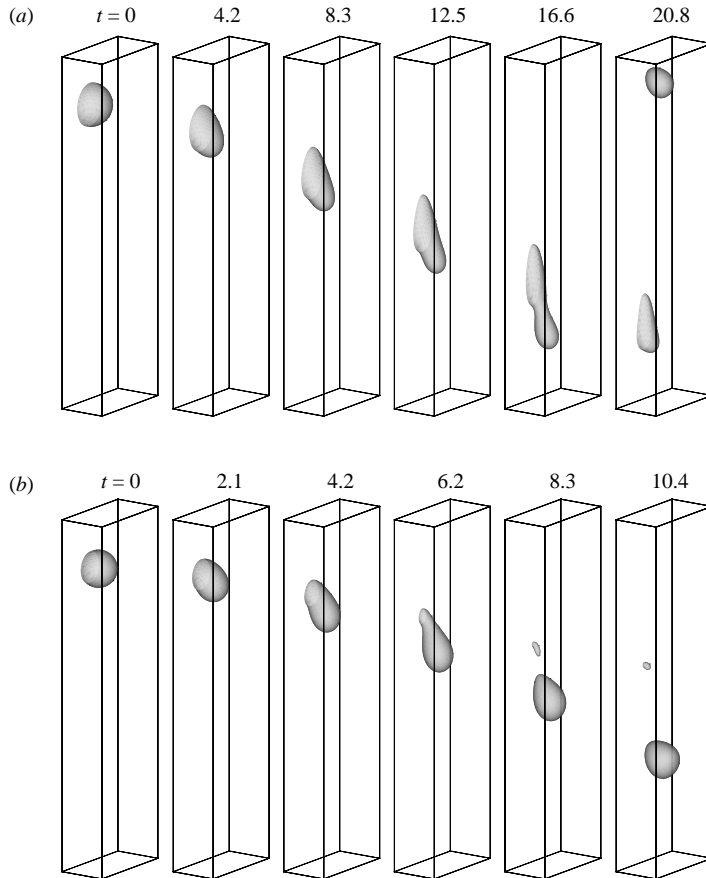


FIGURE 8. Dynamic behaviour of the droplet at $Ca = 0.50$ (three-dimensional view): (a) $\theta = 90^\circ$, (b) $\theta = 118^\circ$. Part of the droplet pinches off for both cases. In (a), the detached portion re-enters the system owing to the periodic conditions applied along the z -direction.

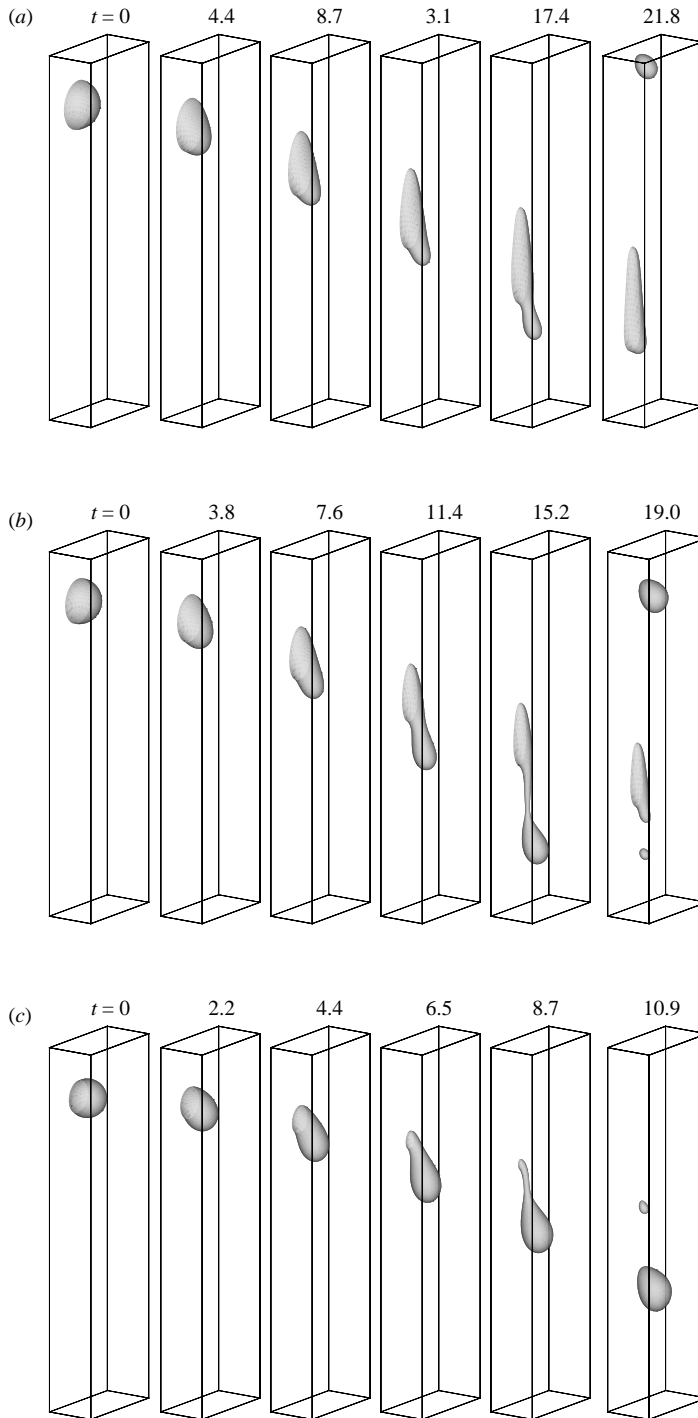


FIGURE 9. Dynamic behaviour of the droplet at $Ca=0.66$ (three-dimensional view), corresponding to figure 5: (a) $\theta = 78^\circ$, a small portion of the droplet pinches off from the rest, (b) $\theta = 90^\circ$, two small droplets pinch off from the rest in tandem, (c) $\theta = 118^\circ$, a large portion of the droplet pinches off, and the rest detaches from the wall.

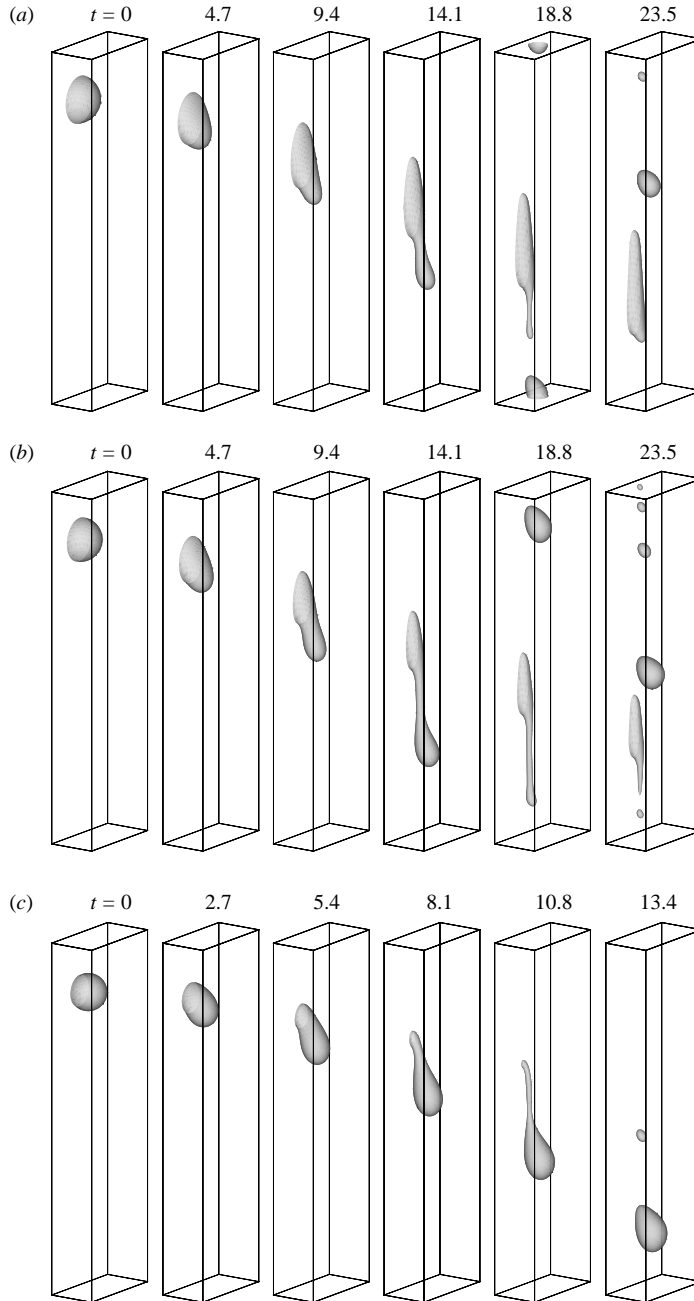


FIGURE 10. Dynamic behaviour of the droplet at $Ca=0.81$ (three-dimensional view), corresponding to figure 6: (a) $\theta = 78^\circ$, two small droplets pinch off from the rest in tandem, (b) $\theta = 90^\circ$, a number of small droplets break from the original droplet and are entrained into the bulk fluid, (c) $\theta = 118^\circ$, a large portion of the droplet pinches off, and the rest detaches from the wall.

(Ca_c), below which a sliding droplet with a constant shape may be observed, and above which no steadily sliding droplet will be obtained. This result is in line with the two-dimensional simulation.

At the capillary number of 0.50 (figure 4), for the wetting case, both b/b_0 and A/A_0 vary similarly as they do at the capillary number of 0.35, but with larger magnitude. For $\theta = 90^\circ$, the wetted length increases continuously before a portion of the droplet pinches off and is entrained into the bulk flow, as shown in figure 8(a). Then, the wetted length begins to decrease. The wetted area, however, decreases monotonically all the time. This change of wetted length at a capillary number above the critical value is different from the results of the two-dimensional simulations, which show that the droplet spreads along the wall at first and then shrinks, and that the downstream part of the droplet pinches off when the droplet is shrinking. For the non-wetting case, both wetted length and wetted area quickly decrease with time before a large portion of the droplet is entrained into the displacing fluid. The rest of the droplet is still attached to the wall (see figure 8b). Therefore, the wetted length and wetted area will not reach zero.

Since the capillary number of 0.66 (figure 5) is greater than the critical capillary number of all three cases, no steadily sliding droplet is observed. However, the droplet with different static contact angles behaves very differently (see figure 9). For $\theta = 78^\circ$, the wetted length increases continuously and a small portion of the droplet breaks off at its peak value. Then the wetted length begins to decrease. The wetted area, however, increases monotonically all the time. For $\theta = 90^\circ$, the wetted length increases monotonically. The wetted area first increases slightly and then decreases steadily before it becomes stable. A larger portion pinches off at time 15.6 and a smaller one at time 18.8. For $\theta = 118^\circ$, both b/b_0 and A/A_0 steadily decrease with time and reach 0 at time 11. However, the droplet does not detach from the wall as a whole, as in the case of capillary number 0.35. Instead, a larger portion pinches off first, as in the case of capillary number 0.50, and the rest detaches from the wall subsequently (see figure 9c).

As the capillary number further increases to 0.81 (figure 6), the wetted length grows monotonically for the wetting droplet, while the wetted area goes up and down. Two small droplets pinch off from the original droplet in tandem, as shown in figure 10(a). The first detachment corresponds to a local minimum of the wetted area. For $\theta = 90^\circ$, both b/b_0 and A/A_0 change similarly to the way they do at capillary number 0.66. However, as shown in figure 10(b), a number of small droplets break from the original droplet and are entrained into the bulk flow. The non-wetting droplet behaves similarly to the way it does at capillary number 0.66: a larger portion pinches off first, and then the rest detaches from the wall, as shown in figure 10(c).

When the first portion pinches off, the rest of the droplet has a smaller size and hence, a smaller capillary number. We may expect it to recover to the behaviour of the droplet with the same contact angle and at a reduced capillary number. However, because their initial conditions are different, the behaviour of the remaining portion should depend greatly on the process. Let us take the non-wetting displacement as an example, for the capillary numbers 0.66 and 0.81, the remaining portion detaches from the wall in both cases. However, it may not detach from the wall if it starts moving from a static droplet under the same strength of gravity.

In general, the wetted length and wetted area change in the same direction for $\theta = 78^\circ$ and $\theta = 118^\circ$, but in the opposite direction for $\theta = 90^\circ$, as shown in figures 3–6.

Figure 11 is the (x, z) -plane view of the dynamical behaviour of the droplet at the three contact angles and at capillary number 0.66. The (x, z) -plane is at the wall where $y = 0$. From this figure, we can see the shape of the fluid/solid interface between the droplet and the wall at different time steps. For $\theta = 78^\circ$, both wetted length and wetted area increase with time, as shown more clearly in figure 5, but the normalized wetted length is always greater than the normalized wetted area. As a

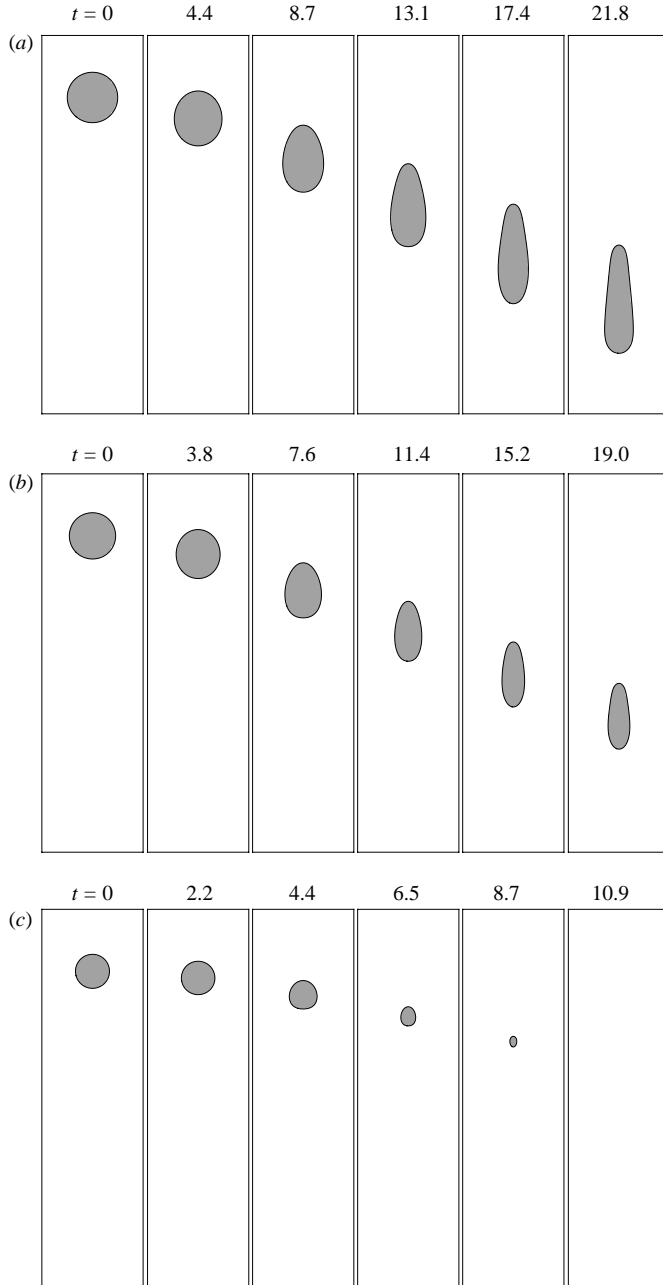


FIGURE 11. Dynamic behaviour of the droplet at $Ca=0.66$ ((x, z) -plane view):
 (a) $\theta = 78^\circ$, (b) $\theta = 90^\circ$, (c) $\theta = 118^\circ$.

result, the wetted width (in the x -direction) decreases. For $\theta = 90^\circ$, the wetted length increases while the wetted area decreases, as shown in figure 5. Therefore, the wetted width decreases more to compensate. In both cases, the shape of the interface is distorted severely. For $\theta = 118^\circ$, both wetted length and wetted area decrease, and so does the wetted width in the x -direction. The round shape of the interface remains almost unchanged when the wetted area diminishes.

	$Ca=0.35$	$Ca=0.50$	$Ca=0.66$	$Ca=0.81$
$\theta = 78^\circ$			0.256	0.341
$\theta = 90^\circ$		0.543	0.574	0.577
$\theta = 118^\circ$	1.0	0.988	0.977	0.973

TABLE 1. The volume ratio of the first detached droplet to the whole droplet.

From figures 9 and 10, or from table 1, we can see that at a certain capillary number, the size of the first detached droplet is largest for $\theta = 118^\circ$ and smallest for $\theta = 78^\circ$. This result confirms the conclusion obtained in our two-dimensional simulation and the assertion by Schleizer & Bonnecaze (1998) that increasing the contact angle results in a larger fraction of the droplet being entrained in the bulk. We can also see from table 1 that increasing the capillary number results in an increase of the size of the first detached droplet for $\theta = 78^\circ$ and $\theta = 90^\circ$, but in a decrease for $\theta = 118^\circ$.

Figure 12 shows the velocity fields of the detaching process in an (y, z) -plane. This plane is the symmetrical plane where $x = 40$. Note that the no-slip boundary condition is satisfied well at the wall. We can see that when $\theta = 78^\circ$ and 90° , the velocity inside the downstream part of the droplet is larger than that inside the upstream part, which causes the downstream part to translate more rapidly and eventually pinch off from the upstream part. When $\theta = 118^\circ$, however, the velocity inside the droplet is almost uniform and larger than that of fluid 1 near the wall. That means the shear forces between the droplet and the wall are very large and eventually cause the entire droplet to detach from the wall.

Figure 13 shows the velocity field in the symmetrical plane and relative to the average droplet velocity when the droplet is steadily sliding. It reveals a vortex flow pattern within the droplet itself in this plane, which is very similar to that obtained in two-dimensional simulations by Kang *et al.* (2002) and by Grubert & Yeomans (1999).

Figure 14 shows the dependence of the critical capillary number on the static contact angle. For each contact angle, a large number of simulations are required to find the critical value of the body force through interpolation. Therefore, we calculate the critical capillary number for only five contact angles because of the extensive computational efforts. However, it is sufficient to confirm the general trend found in the two-dimensional study (Kang *et al.* 2002) that the critical capillary number decreases as the contact angle increases.

There is a family of $g_{k\bar{k}}$ and g_{kw} terms that give the same contact angle. In a simulation not shown here, we increased g_{12} , but kept $g_{11} = g_{22} = 0$ (hence the contact angle is fixed at 90°). As a result, the surface tension increases, and so does the body force strength required for detachment. Thus, the critical capillary number remains nearly unchanged, and the droplet behaves very similarly. However, the interface width decreases as the increase of g_{12} , and how this width affects the dynamics of flow near the moving contact line requires further scrutiny.

5. Effect of capillary number

Figures 15 and 16 illustrate the dependency of the steady-state value of the non-dimensional wetted length b/b_0 and wetted area A/A_0 on the capillary number Ca , respectively. Different capillary numbers are obtained by changing g , the gravitational

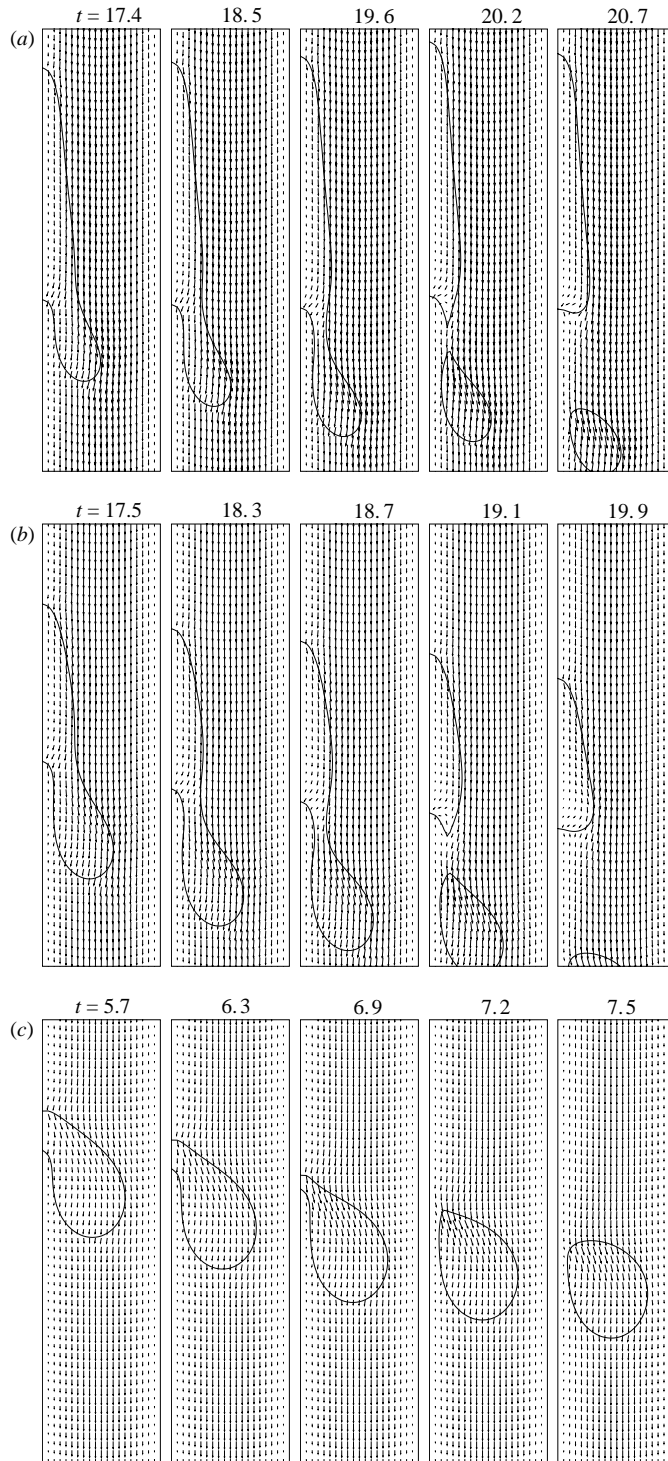


FIGURE 12. Velocity fields of the detaching process in the symmetrical plane $x = 40$: (a) $\theta = 78^\circ$ and $Ca = 0.66$, (b) $\theta = 90^\circ$ and $Ca = 0.50$, (c) $\theta = 118^\circ$ and $Ca = 0.35$.

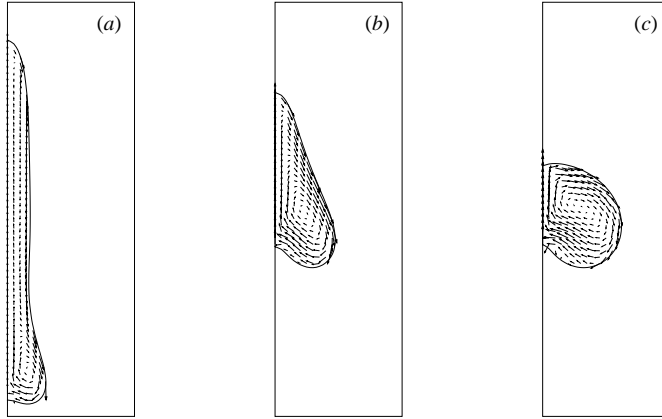


FIGURE 13. Velocity profile within the droplet minus average droplet velocity: (a) $\theta = 78^\circ$ at $Ca = 0.62$, (b) $\theta = 90^\circ$ at $Ca = 0.46$, (c) $\theta = 118^\circ$ at $Ca = 0.15$.

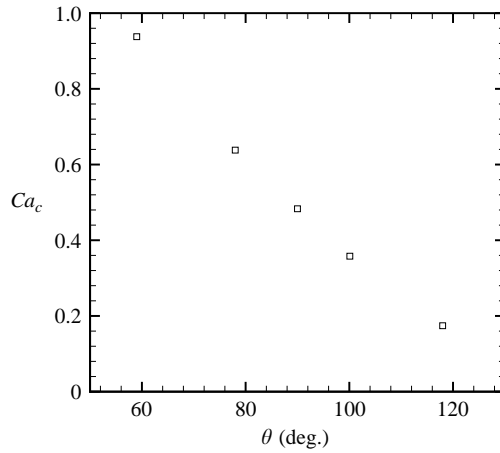


FIGURE 14. Dependency of the critical capillary number (Ca_c) on the contact angle (θ).

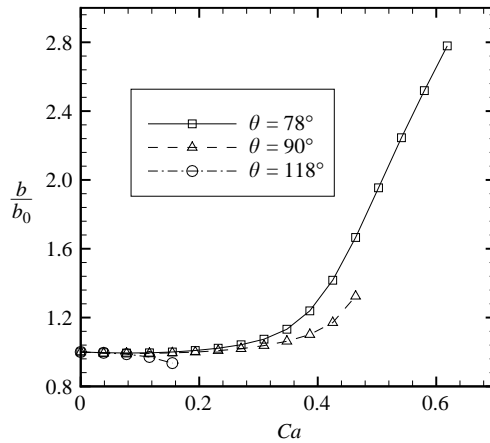


FIGURE 15. Dependency of the steady-state wetted length between the droplet and the wall on the capillary number.

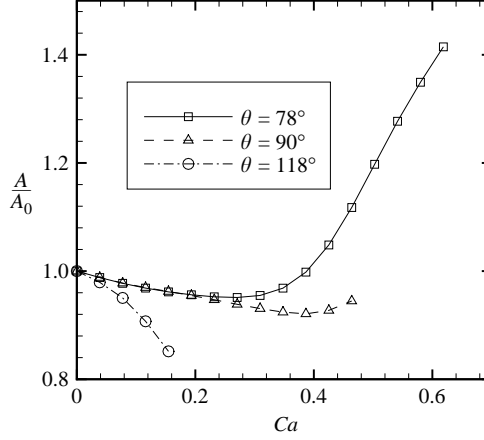


FIGURE 16. Dependency of the steady-state wetted area between the droplet and the wall on the capillary number.

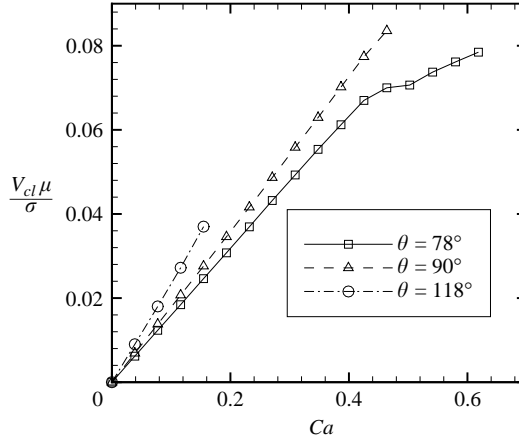


FIGURE 17. Dependency of the steady-state contact-line velocity on the capillary number.

factor. For $\theta = 78^\circ$ and $\theta = 90^\circ$, and when Ca is small, b/b_0 remains at 1 while A/A_0 decreases with the increase of Ca . As Ca increases further, both b/b_0 and A/A_0 increase. The increase of b/b_0 is greater in magnitude than its two-dimensional counterpart, because the wetted width (in x -direction) of the three-dimensional droplet can decrease to compensate. For the non-wetting droplet, both b/b_0 and A/A_0 decrease with time monotonically until Ca exceeds the critical value.

Figure 17 shows the dependency of the steady-state value of the dimensionless contact-line velocity $\mu V_{cl}/\sigma$ (or the droplet velocity, since the shape of the droplet does not change with time any more) on the capillary number. For $\theta = 90^\circ$ or $\theta = 118^\circ$, this velocity is linear in Ca , meaning that the droplet translates more rapidly as Ca increases. The slope for $\theta = 90^\circ$ is smaller than that for $\theta = 118^\circ$. For the wetting case, however, there are two regions where the contact-line velocity varies linearly. The transition between these regions is about $0.39 \leq Ca \leq 0.50$, which corresponds to the region where both b/b_0 and A/A_0 increase rapidly, as seen in figures 15 and 16, and thus corresponds to the region where the droplet shape changes significantly, as seen in figures 18(a) and 19(a). Figures 18 and 19 are the (x, z) - and (y, z) -plane views

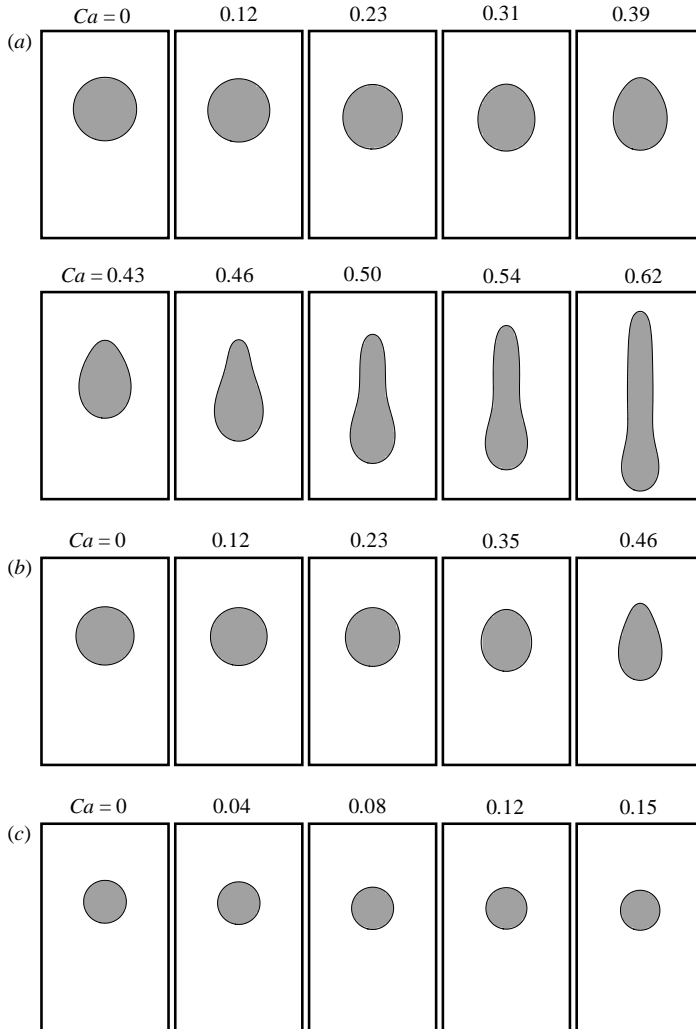


FIGURE 18. The steady-state shape of the droplet at different capillary numbers ((x, z)-plane view at wall): (a) $\theta = 78^\circ$, (b) $\theta = 90^\circ$, (c) $\theta = 118^\circ$.

of the steady-state shape of the droplet at different capillary numbers, respectively. From figure 18, we can see that the interface between the non-wetting droplet and the wall keeps its round shape. For the other two contact angles, however, the interface deviates from its original round shape, and the larger the capillary number, the greater this deviation. We can also see from figures 18 and 19 that the steady-state shape of the droplet is greatly stretched from its original static shape, especially for $\theta = 78^\circ$ and $\theta = 90^\circ$, and the larger the capillary number, the greater the stretch.

Since no assumption about the relationship between the contact angle and velocity of the contact line is required in our study, the steady-state shapes of the droplets (see figure 19) look different from those of the droplets in simulations by Schleizer & Bonnecaze (1998), where the contact angle is assumed to be independent of the speed of the contact line and equal to its static value. Instead, the droplet shapes here are similar to those of the static droplets in simulations by Dimitrakopoulos & Higdon (2001) with contact angle hysteresis.

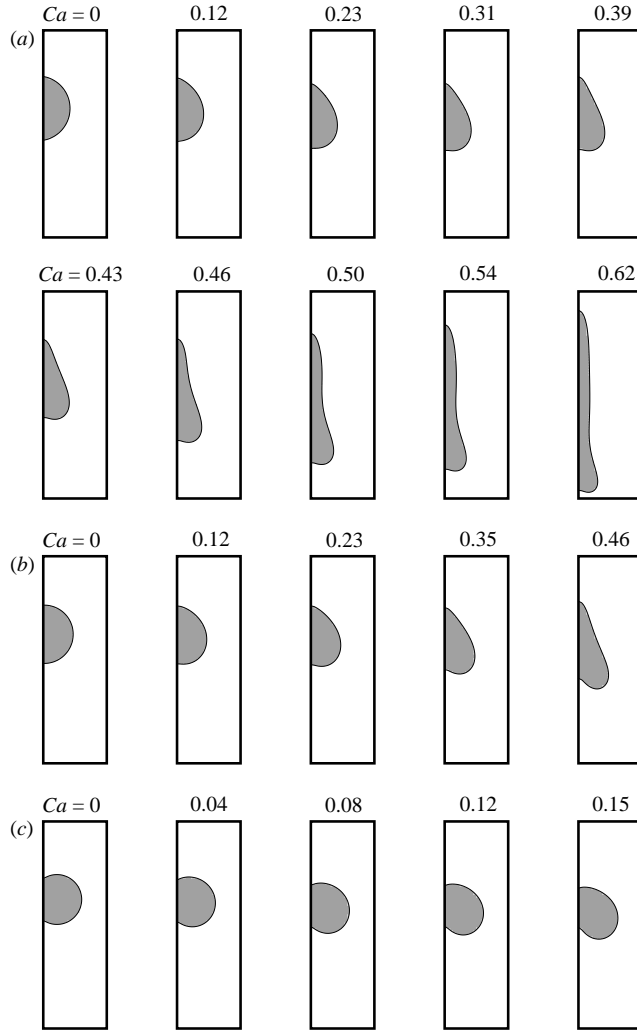


FIGURE 19. The steady-state shape of the droplet at different capillary numbers ((y, z)-plane view at $x = 40$): (a) $\theta = 78^\circ$, (b) $\theta = 90^\circ$, (c) $\theta = 118^\circ$.

Figure 20 shows the time evolution of the bottleneck area at the three contact angles and different capillary numbers. The bottleneck area is defined as the minimal horizontal area between the up- and downstream parts of the droplet and is normalized by the initial wetted area. The first and last time instants correspond to the initial formation of the bottleneck and the final detachment of the downstream part, respectively. It is clear that this area decreases with time for all contact angles and capillary numbers shown. For the highest capillary number ($Ca = 0.81$), the bottleneck area changes with time nearly exponentially for all contact angles. For a certain contact angle, the decrease of the bottleneck area slows down with time as the capillary number goes up. In other words, the larger the capillary number, the longer the time between the initial formation of the bottleneck and the final detachment of the downstream part of the droplet. This phenomenon implies that at a larger capillary number, the droplet is stretched farther before it breaks down.

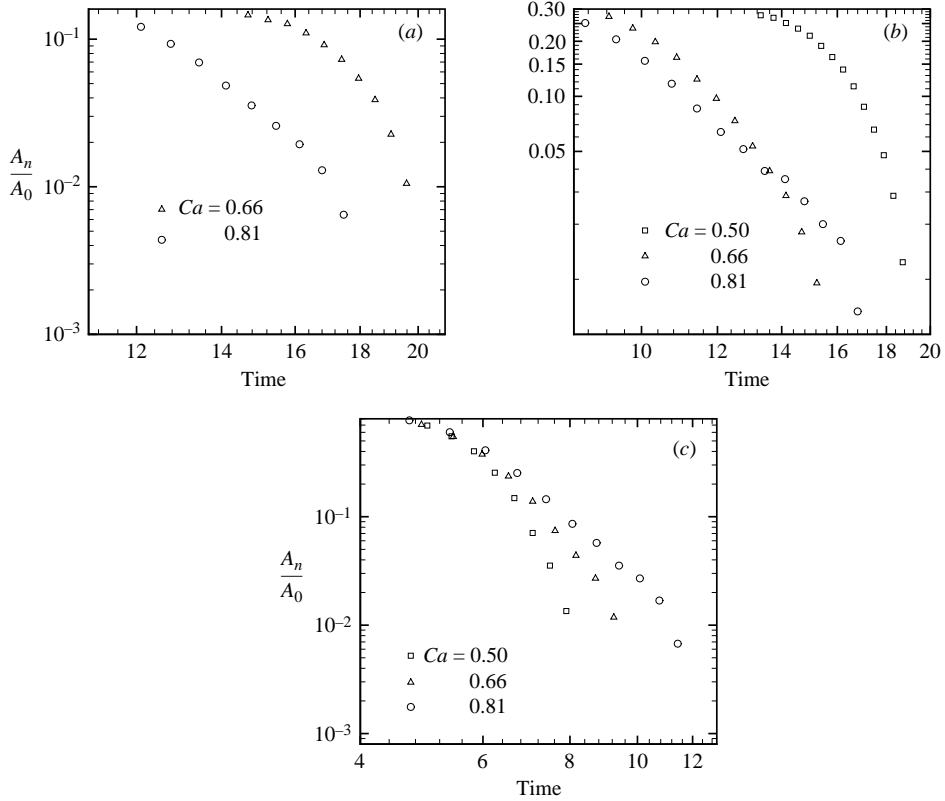


FIGURE 20. Time evolution of the normalized bottleneck area: (a) $\theta = 78^\circ$, (b) $\theta = 90^\circ$, (c) $\theta = 118^\circ$.

This conclusion can be drawn directly from figures 8–10 and can also be confirmed by figure 21, which shows the time evolution of the normalized mass-centre velocity of the up- and downstream parts of the droplet, delimited by the bottleneck. The solid symbols designate the downstream part and the open symbols the upstream part. The area between them indicates the change of the distance between the mass centres of the two parts, which is an indication of how much the droplet is stretched. It is clear that the larger the capillary number is, the farther the droplet is stretched.

We can also see from figure 21 that the mass-centre velocity of the downstream part increases steadily with time, but that of the upstream part tends to change with time irregularly as the capillary number or the contact angle increases. One possible reason for this effect of the contact angle is that as it increases, the volume of the upstream part becomes smaller and hence more sensitive to the location of the border between the two parts. One explanation for this effect of the capillary number is that at a high capillary number, the upstream part may become unstable. This instability will be the subject of a future study.

Figure 22 shows the velocity vector and speed distribution (normalized by characteristic velocity $U = \rho_1 g h^2 / \mu_1$) at the droplet surface with $\theta = 90^\circ$, $Ca = 0.66$, $t = 15.2$ and $Re = 19.05$. The Reynolds number is defined as $Re = \bar{W}h/\nu$, where \bar{W} is the average velocity along the $-z$ -direction in the whole domain at this time instant. The red colour indicates the high value of the speed and the blue colour the low value. It is clear that the speed is generally larger in the downstream part than in the upstream

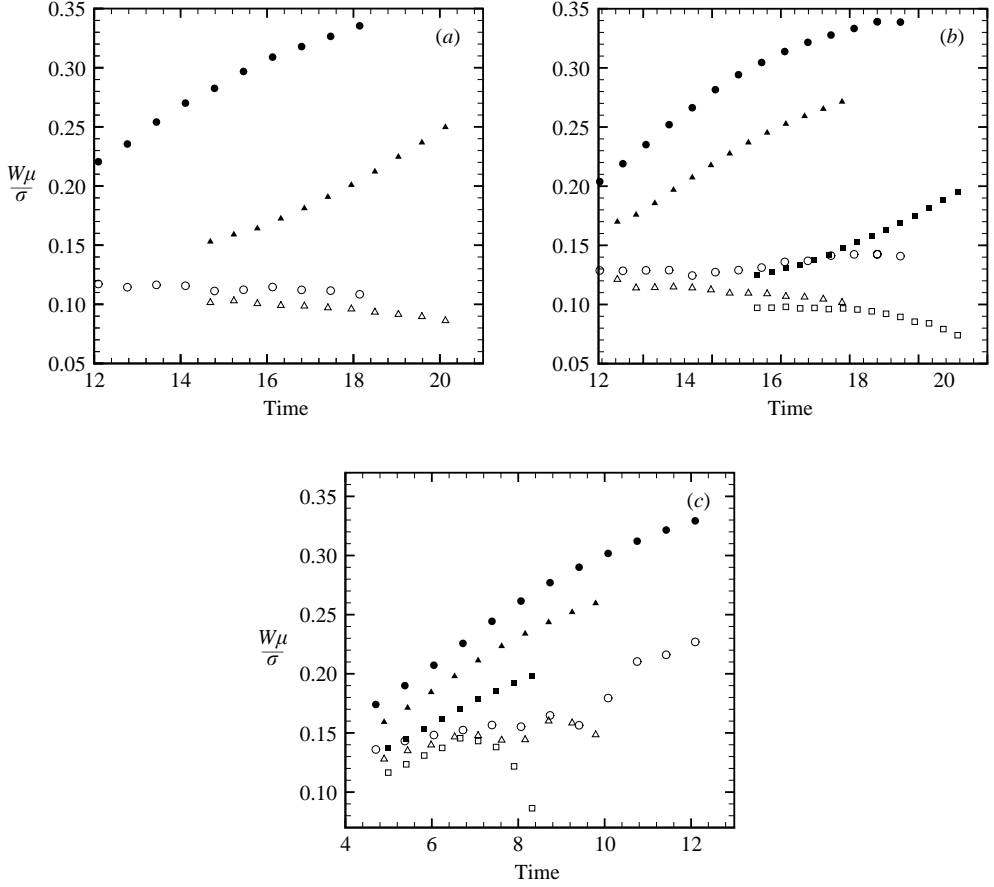


FIGURE 21. Time evolution of the normalized mass-centre velocity of the up- and downstream parts of the droplet. The solid symbols designate the downstream part and the open symbols the upstream part. \square and \blacksquare : $Ca = 0.50$; \triangle and \blacktriangle : $Ca = 0.66$; \circ and \bullet : $Ca = 0.81$: (a) $\theta = 78^\circ$, (b) $\theta = 90^\circ$, (c) $\theta = 118^\circ$.

part. The maximum speed occurs near the bottleneck rather than at the far end of the downstream part. The reason is that the droplet is quickly stretched and hence the velocity is very large near the bottleneck.

Figure 23 shows the distribution of the shear stress τ_{yz} (normalized by $\rho_1 U^2$, where U is the characteristic velocity) in the vicinity of the droplet. The shear stress is calculated based on the constitutive assumption for Newtonian fluids (i.e. $\tau_{yz} = \mu((\partial u_z/\partial y) + (\partial u_y/\partial z))$, where μ is the dynamic viscosity, and u_y and u_z are velocity components in the y - and z -directions, respectively), although the fluid mixture near the fluid/fluid interface would probably be non-Newtonian owing to the finite interface thickness (Dussan V. & Davis 1974). The velocity derivatives in the expression of τ_{yz} are calculated using second-order finite-difference methods. The negative peak is at the advancing contact line, which is consistent with the result of the atomistic simulation of flow in the vicinity of the advancing and receding solid–liquid–vapour contact lines of a two-dimensional (in the mean) liquid drop, which is in thermodynamic equilibrium with its own vapour and moves steadily owing to an applied body force (Freund 2003). The absolute value of the negative peak in our study is about three times that of the positive peak, which occurs at the other wall ($y = 40$).

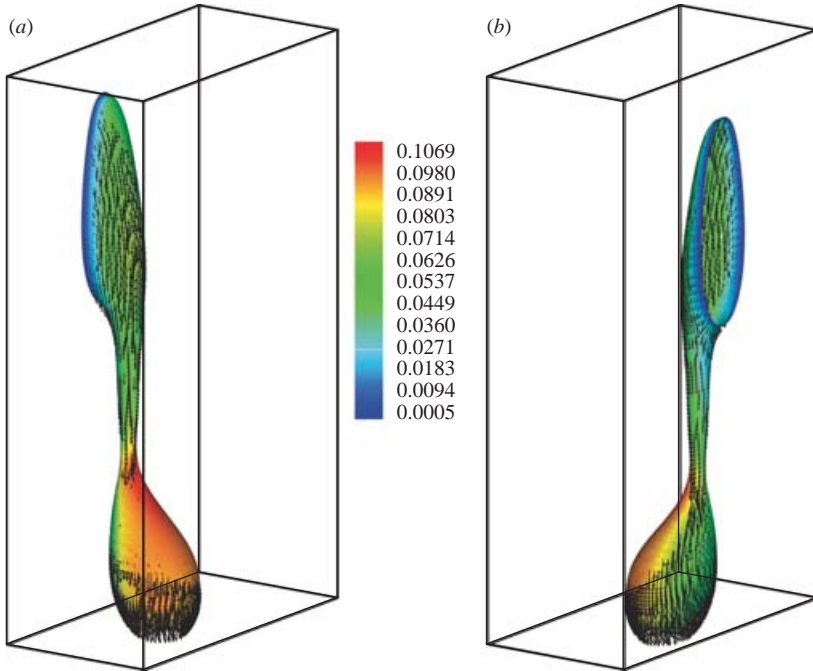


FIGURE 22. (a) Velocity vector and speed distribution at the droplet surface with $\theta = 90^\circ$, $Ca = 0.66$, $t = 15.2$ and $Re = 19.05$. (b) The same as (a), but in different view angle.

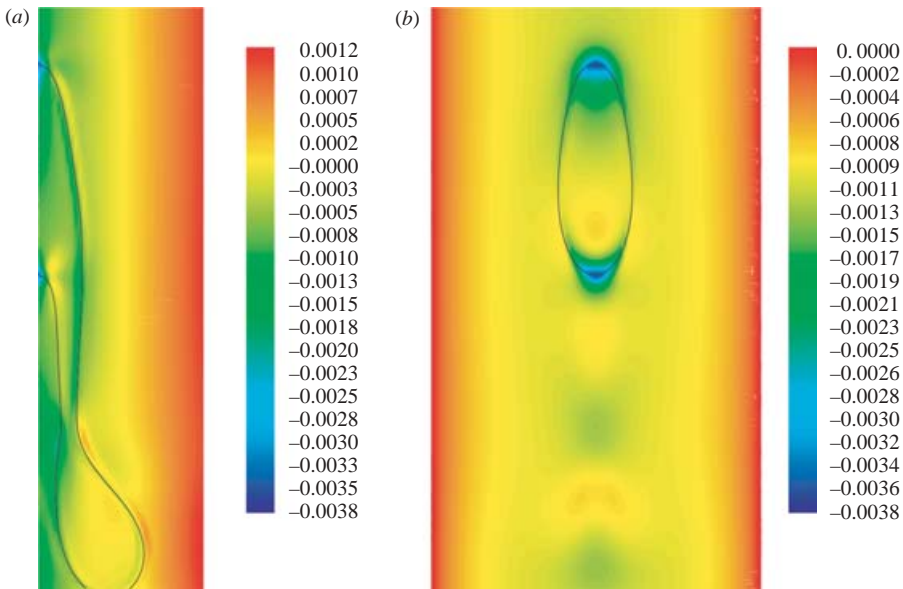


FIGURE 23. Distribution of the shear stress τ_{yz} in the vicinity of the droplet with $\theta = 90^\circ$, $Ca = 0.66$, $t = 15.2$ and $Re = 19.05$: (a) in the (y, z) -plane at $x = 40$, (b) in the (x, z) -plane at the wall.

It is also seen from figure 23(a) that at the bottleneck where the velocity peaks, both the negative shear stress at the left of the bottleneck and its positive counterpart at the right reach their local maxima. This indicates that the droplet at the bottleneck

is undergoing very large stretch, which results in the eventual break of the bottleneck and therefore the detachment of the downstream part of the droplet.

6. Conclusions

We have simulated the displacement of a three-dimensional immiscible droplet of various wettabilities in a duct by the lattice Boltzmann method. The driving force is the gravitational forces. It has been found that there exists a critical capillary number, under which the droplet would move along the wall and reach a steady state.

At a capillary number just above the critical value, a small portion would pinch off from the rest of the droplet for $\theta = 78^\circ$ and a large portion for $\theta = 90^\circ$. The rest would still attach to the wall. For $\theta = 118^\circ$, however, the entire droplet would detach from the wall. When the capillary number further increased, more than one small droplet would pinch off for $\theta = 78^\circ$ and $\theta = 90^\circ$, and the rest would still adhere to the wall. For the non-wetting droplet, however, a large portion would break off first and the rest would detach from the wall if the capillary number was large enough. In a previous two-dimensional simulation, we did not increase the capillary number so much after it exceeded the critical value so that we observed only the first detachment.

At a fixed capillary number above the critical value, increasing the contact angle resulted in a larger first-detached droplet, which also agreed with the two-dimensional study. The current study also confirmed the general trend found in the two-dimensional study that the critical capillary number decreased as the contact angle increased.

In the detaching process, the wetted length and wetted area varied in the opposite direction for the droplet with $\theta = 90^\circ$, and hence the wetted shape was distorted most. For the droplet with $\theta = 118^\circ$, both wetted length and wetted area decreased and the round shape of the fluid/solid interface remained almost unchanged when the wetted area diminished.

In the non-wetting displacement, both the steady-state wetted length and wetted area decreased monotonically and the steady-state velocity of the contact lines increased linearly as the capillary number increased. For the case of a contact angle less than or equal to 90° , the situation was more complicated. The steady-state wetted length and wetted area remained unchanged or decreased at first, and then both increased as the capillary number increased. When $\theta = 90^\circ$, the steady-state velocity of the contact lines also increased linearly with the increase of the capillary number, but with a smaller slope than when $\theta = 118^\circ$. When $\theta = 78^\circ$, however, the steady-state contact-line velocity varied linearly in two regions. The transition between the two regions corresponded to the region where there was a great change in the droplet shape.

When $\theta = 118^\circ$, the steady-state interface between the droplet and the wall kept its round shape. For the other two cases, however, the interface deviated from the original circular shape as the capillary number increased.

A displaced droplet was stretched longer when the capillary number was larger. When part of the droplet was detaching, the maximal value of the velocity at the fluid/fluid interface occurred near the bottleneck instead of the far end of the downstream droplet, and the shear stress at the bottleneck reaches a local maximum.

The stability of the droplet and the distribution of stress and strain in the detaching process constitute topics for our future work.

This work was partially funded by LDRD/DR Projects 20030059, 20040042 and IGPP Project 1300, all sponsored by Los Alamos National Laboratory, which is

operated by the University of California for the US Department of Energy. S. C.'s research was supported by China's NSF (10128204).

REFERENCES

- BRIANT, A. J., WAGNER, A. J. & YEOMANS, J. M. 2004 Lattice Boltzmann simulations of contact line motion. I. Liquid–gas systems. *Phys. Rev. E* **69**, 031602–031602.
- BRIANT, A. J. & YEOMANS, J. M. 2004 Lattice Boltzmann simulations of contact line motion. II. Binary fluids. *Phys. Rev. E* **69**, 031603–031603.
- CHEN, H., CHEN, S. & MATTHAEUS, W. H. 1992 Recovery of the Navier–Stokes equations using a lattice-gas Boltzmann method. *Phys. Rev. A* **45**, R5339–R5342.
- CHEN, H. Y., JASNOW, D. & VINALS, J. 2000 Interface and contact line motion in a two phase fluid under shear flow. *Phys. Rev. Lett.* **85**, 1686–1689.
- CHEN, S. & DOOLEN, G. D. 1998 Lattice Boltzmann method for fluid flows. *Annu. Rev. Fluid Mech.* **30**, 329–364.
- COX, R. G. 1986 The dynamics of the spreading of liquids on a solid surface. *J. Fluid Mech.* **168**, 169–194.
- DIMITRAKOPOULOS, P. & HIGDON, J. J. L. 2001 On the displacement of three-dimensional fluid droplets adhering to a plane wall in viscous pressure-driven flows. *J. Fluid Mech.* **435**, 327–350.
- DUSSAN V., E. B. 1976 The moving contact line: the slip boundary condition. *J. Fluid Mech.* **77**, 665–684.
- DUSSAN V., E. B. 1979 On the spreading of liquids on solid surfaces: static and dynamic contact lines. *Annu. Rev. Fluid Mech.* **11**, 371–400.
- DUSSAN V., E. B. & DAVIS, S. H. 1974 On the motion of a fluid–fluid interface along a solid surface. *J. Fluid Mech.* **65**, 71–95.
- FREUND, J. B. 2003 The atomic detail of a wetting/de-wetting flow. *Phys. Fluids* **15**, L33–L36.
- DE GENNENS, P. G. 1985 Wetting: statics and dynamics. *Rev. Mod. Phys.* **57**, 827–863.
- GRUBERT, D. & YEOMANS, J. M. 1999 Mesoscale modeling of contact line dynamics. *Comput. Phys. Comm.* **121–122**, 236–239.
- GUNSTENSEN, A. D., ROTHMAN, D. H., ZALESKI, S. & ZANETT, G. 1991 Lattice Boltzmann model of immiscible fluids. *Phys. Rev. A* **43**, 4320–4327.
- HE, X., CHEN, S. & ZHANG, R. 1999a A lattice Boltzmann scheme for incompressible multiphase flow and its application in simulation of Rayleigh–Taylor instability. *J. Comput. Phys.* **152**, 642–663.
- HE, X. & DOOLEN, G. D. 2002 Thermodynamic foundation of kinetic theory and lattice Boltzmann models for multiphase flow. *J. Stat. Phys.* **107**, 309–328.
- HE, X., ZHANG, R., CHEN, S. & DOOLEN, G. D. 1999b On the three-dimensional Rayleigh–Taylor instability. *Phys. Fluids* **11**, 1143–1152.
- HOCKING, L. M. 1976 A moving fluid interface on a rough surface. *J. Fluid Mech.* **76**, 801–817.
- HOCKING, L. M. 1977 A moving fluid interface. Part 2. The removal of the force singularity by a slip flow. *J. Fluid Mech.* **79**, 209–229.
- HOU, S., SHAN, X., ZOU, Q., DOOLEN, G. D. & SOLL, W. 1997 Evaluation of two lattice Boltzmann models for multiphase flows. *J. Comput. Phys.* **138**, 695–713.
- JACQMIN, D. 2000 Contact-line dynamics of a diffuse fluid interface. *J. Fluid Mech.* **402**, 57–88.
- JANSONS, K. M. 1985 Moving contact lines on a two-dimensional rough surface. *J. Fluid Mech.* **154**, 1–28.
- KANG, Q., ZHANG, D. & CHEN, S. 2002 Displacement of a two-dimensional immiscible droplet in a channel. *Phys. Fluids* **14**, 3203–3214.
- KOPLIK, J., BANAVAR, J. R. & WILLEMSEN, J. F. 1988 Molecular dynamics of a Poiseuille flow and moving contact lines. *Phys. Rev. Lett.* **60**, 1282–1285.
- MARTYS, N. S. & CHEN, H. 1996 Simulation of multicomponent fluids in complex three-dimensional geometries by the lattice Boltzmann method. *Phys. Rev. E* **53**, 743–750.
- NIE, X., DOOLEN, G. D. & CHEN, S. 2002 Lattice-Boltzmann simulations of fluid flows in MEMS. *J. Stat. Phys.* **107**, 279–289.

- SCHLEIZER, A. D & BONNECAZE, R. T. 1998 Displacement of a two-dimensional immiscible droplet adhering to a wall in shear and pressure-driven flows. *J. Fluid Mech.* **383**, 29–54.
- SHAN, X. & CHEN, H. 1993 Lattice Boltzmann model for simulation flows with multiple phases and components. *Phys. Rev. E* **47**, 1815–1819.
- SHAN, X. & DOOLEN, G. D. 1995 Multicomponent lattice-Boltzmann model with interparticle interaction. *J. Stat. Phys.* **81**, 379–393.
- SHAN, X. & DOOLEN, G. D. 1996 Diffusion in a multicomponent lattice Boltzmann equation model. *Phys. Rev. E* **54**, 3614–3620.
- SHIKHMURZAEV, Y. D. 1997 Moving contact lines in liquid/liquid/solid systems. *J. Fluid Mech.* **334**, 211–249.
- SWIFT, M., OSBORN, W. & YEOMANS, J. 1995 Lattice Boltzmann simulation of nonideal fluids. *Phys. Rev. Lett.* **75**, 830–833.
- WOLFRAM, S. 1986 Cellular automaton fluids. 1: Basic theory. *J. Stat. Phys.* **45**, 471–526.
- YANG, Z. L., DINH, T. N., NOURGALIEV, R. R. & SEHGAL, B. R. 2000 Numerical investigation of bubble coalescence characteristics under nucleate boiling condition by a lattice-Boltzmann model. *Intl J. Therm. Sci.* **39**, 1–17.
- ZHOU, M. Y. & SHENG, P. 1990 Dynamics of immiscible fluid displacement in a capillary tube. *Phys. Rev. Lett.* **64**, 882–885.